Exploration of all-3*d* Heusler alloys for permanent magnets:
An *ab initio* based high-throughput study

Madhura Marathe ●[*] and Heike C. Herper ●

Department of Physics and Astronomy, Uppsala University, 751 20 Uppsala, Sweden

Heusler alloys have attracted interest in various fields of functional materials since their properties can quite easily be tuned by composition. Here, we have investigated the relatively new class of all-3*d* Heusler alloys in view of their potential as permanent magnets. To identify suitable candidates, we performed a high-throughput study using an electronic structure database to search for X_2YZ-type Heusler systems with tetragonal symmetry and high magnetization. For the alloys which passed our selection filters, we have used a combination of density functional theory calculations and spin dynamics modeling to investigate their magnetic properties including the magnetocrystalline anisotropy energy and exchange interactions. The candidates which fulfilled all the search criteria served as input for the investigation of the temperature dependence of the magnetization and determination of the Curie temperature. Based on our results, we suggest that Fe_2NiZn, Fe_2NiTi, and Ni_2CoFe are potential candidates for permanent magnets with large out-of-plane magnetic anisotropy (1.23, 0.97, and 0.82 MJ/m^3, respectively) and high Curie temperatures lying more than 200 K above the room temperature. We further show that the magnitude and direction of anisotropy are very sensitive to the strain by calculating the values of anisotropy energy for several tetragonal phases. Thus application of strain can be used to tune the anisotropy in these compounds.

I. INTRODUCTION

The discovery of new magnetic materials is vital to improve the performance of a range of applications from data storage to renewable energy sources [1]. Permanent magnets constitute an essential component of electric generators used in wind turbines, and a large amount of magnetic material is required for each generator [2,3]. Most commonly used permanent magnets in current devices typically contain rare-earth elements such as neodymium, samarium, etc., which make these materials expensive, and on top of that their mining is usually harmful to the environment [4]. Therefore alternative candidates for permanent magnets are highly sought after to improve the overall sustainability. We would like to note that there is an intrinsic limit on the functional response of permanent magnets consisting of light elements determined by associated small spin-orbit coupling [5]. However, we expect that such magnets could replace the rare-earth magnets in midrange applications and thus reduce the overall dependence on rare-earth elements.

What makes a material a good candidate for permanent magnets? A good candidate possesses (1) stability (i.e., it can be synthesized in a given phase and structure; typically, preferred symmetries are tetragonal or hexagonal crystal structures so that there is a single well-defined easy axis), (2) a large magnetic moment, (3) a large magnetocrystalline anisotropy with a preference for out-of-plane magnetization, and (4) a Curie temperature above room temperature, so that the ferromagnetic state is stable at working conditions for devices. Currently, the best strategy to accelerate research into cost-effective and sustainable materials is to use high-throughput methods, that is, to comb through a large number of candidates available in various structural databases for alloys and compounds and then to perform electronic structure calculations to determine the required physical quantities.

Heusler alloys are intermetallic compounds with L2$_1$ structure and typically with the chemical formula X_2YZ. Conventionally, the X and Y elements are 3*d* transition metals, and Z belongs to either group III, IV, or V (main group elements). One advantage of these alloys is the easy tuning of its properties obtained by varying the constituent elements, doping, site disorder, and/or strain making these useful for a multitude of functional properties from shape memory effects and half-metallicity to magnetocaloric response; for a general review on Heusler alloys, see the book edited by Felser and Hirohata [6]. Moreover, a number of studies have reported a large magnetocrystalline anisotropy in Heusler alloys and have also discussed the possibility of its tuning via interstitial doping, strain, and local ordering of atoms [7–10], thus making Heusler alloys ideal potential candidates for permanent magnets.

In recent years, the conventional Heusler family has expanded to include alloys in which all constituent elements

---

are d metals [11]. We mainly focus here on the magnetic properties of this novel class of Heusler compounds, in which Z belongs to the 3d metals, referred to as all-3d Heusler alloys [12–16]. One of the first reports for this type of all-3d Heusler alloy is from Wei *et al.* [12]; in that study, Ni-Mn alloys were doped with Ti to form the Heusler phase, and additional Co doping made the material a strongly ferromagnetic shape memory alloy. Further studies on their functional responses have reported a giant exchange-bias effect [17], a giant barocaloric effect [18], and a large magnetocaloric effect [19,20]. First-principles calculations have predicted the occurrence of martensitic transformation in all-3d Zn_2YMn ($Y =$ Fe, Co, and Ni) alloys [14] as well as high-spin polarization in Fe_2CrZ and Co_2CrZ ($Z =$ Sc, Ti, and V) alloys [16].

In this paper, we examine this new class of materials for potential permanent magnets because most of the 3d metals are abundantly found and show strong magnetic interactions, and there exist well-established routes to make alloys in different phases from these metals, especially binary alloys of Ni-Fe and Fe-Co and ternary alloys based on these alloys [21]. One of the well-studied transition metal alloys is Fe-Co, which has a high saturation magnetization but small magnetocrystalline anisotropy [21]. This alloy has the body-centered cubic (bcc) structure as the most stable phase; however, first-principles calculations have predicted a large anisotropy for Fe-Co in the body-centered tetragonal phase [22,23]. This observation is confirmed by experiments in which stabilization of the tetragonal phase was achieved by either epitaxial growth [24] or doping with another element [25]. Typically, bcc Fe-Co alloys are disordered; however, ordered bulk or thin-film conventional Heusler alloys of the form Fe_2CoZ [26,27] and Co_2FeZ [28,29] ($Z =$ Si or Ga) have been synthesized and reported to have large Curie temperatures.

The main objective of our study is the calculation of the relevant magnetic properties such as magnetocrystalline anisotropy and Curie temperatures for a selected set of all-3d Heusler alloys. It has been shown that strain can be used to tune both the magnitude and the direction of the easy-plane axis in Heusler alloys [8,30]. Thus we also explore possible tuning of the magnetocrystalline anisotropy for selected alloys via strain engineering. The details of our density functional theory calculations and Monte Carlo simulations are given in Sec. II. The selection of suitable candidates is done using an available repository of materials and setting conditions on stability and magnetic moments to filter out materials as described in Sec. III A. The results from our calculations for structural and magnetic properties are presented and discussed in Sec. III B, followed by an analysis of how we can further tune the properties by strain in Sec. III C. Finally, we conclude with a suggestion for a few potential permanent magnets and discuss the general outlook for further theoretical and experimental investigations in Sec. IV.

II. COMPUTATIONAL DETAILS

We perform density functional theory (DFT) calculations using the Vienna *ab initio* simulation package (VASP) code [31] to calculate the structural and magnetic properties of Heusler alloys. We use a 16-atom conventional unit cell for these calculations, shown in Fig. 1(a). For these calcula-
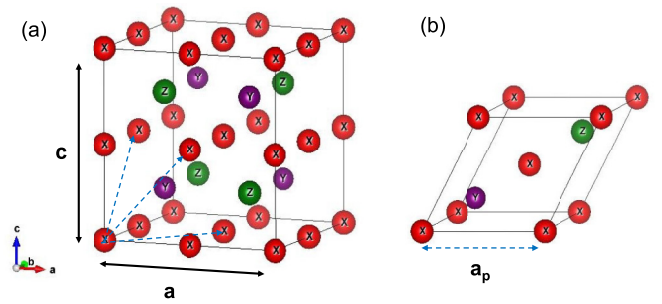

FIG. 1. Unit cells for typical Heusler alloys of the type X_2YZ: conventional 16-atom unit cell (a) and primitive 4-atom unit cell (b). Note that the two unit cells are equivalent and the blue dashed lines shown in (a) correspond to the primitive cell shown in (b). Here, filling of atomic positions corresponds to the "standard" Heusler alloy, whereas the "inverse" structure corresponds to exchange of atoms X and Y occupying positions $(\frac{1}{2}, \frac{1}{2}, \frac{1}{2})$ and $(\frac{1}{4}, \frac{1}{4}, \frac{1}{4})$.

tions, we use an energy cutoff of 650 eV and a k mesh of $16 \times 16 \times 16$. Furthermore, we use the generalized-gradient approximation of the Perdew-Burke-Ernzerhof (PBE) type calculated with the projected augmented-wave (PAW) method [32]. To calculate the magnetic anisotropy energy (MAE) and exchange interactions J_{ij}, we make use of the full-potential linearized muffin-tin orbital (FP-LMTO) code Relativistic Spin Polarized Toolkit (RSPt) [33]. To reduce the computational effort, we use a four-atom primitive unit cell, shown in Fig. 1(b), for these calculations. Furthermore, a dense k mesh of $36 \times 36 \times 36$ is required to accurately capture the smaller energy scale for magnetic interactions. The MAE is calculated using the magnetic force theorem [34] and is given by

$$\mathcal{E}_{\mathrm{MAE}} = E_b^{[100]} - E_b^{[001]}, \tag{1}$$

where E_b^α is the fully relativistic band energy for the magnetization direction α calculated from the self-consistent scalar-relativistic potential. Within this definition, a positive $\mathcal{E}_{\mathrm{MAE}}$ corresponds to the uniaxial anisotropy and therefore indicates a material suitable as a permanent magnet. The exchange parameters are calculated with the Liechtenstein-Katsnelson-Antropov-Gubanov formula [35] as implemented in the RSPt code.

Using the calculated J_{ij}'s, we map our system on a Heisenberg model given by the spin Hamiltonian

$$\mathcal{H} = -\sum_{ij} J_{ij}\mathbf{e}_i.\mathbf{e}_j, \tag{2}$$

where $\mathbf{e}_i$ is a unit vector representing local magnetic moment m_i for site i. Note that the systems considered in this paper contain atoms with partially filled d electrons and typically have long-range exchange interactions extending over several lattice constants. It is essential that we include these in our model to correctly estimate magnetic properties at finite temperatures. We have included pairwise J_{ij}'s for all neighbors j within 4.5a radius from the central site i [36]. We perform Monte Carlo (MC) simulations using the Uppsala Atomistic Spin Dynamics (UppASD) code [37] to obtain finite-temperature properties of the system. Our simulation box has the dimensions $24 \times 24 \times 24$, and three ensembles
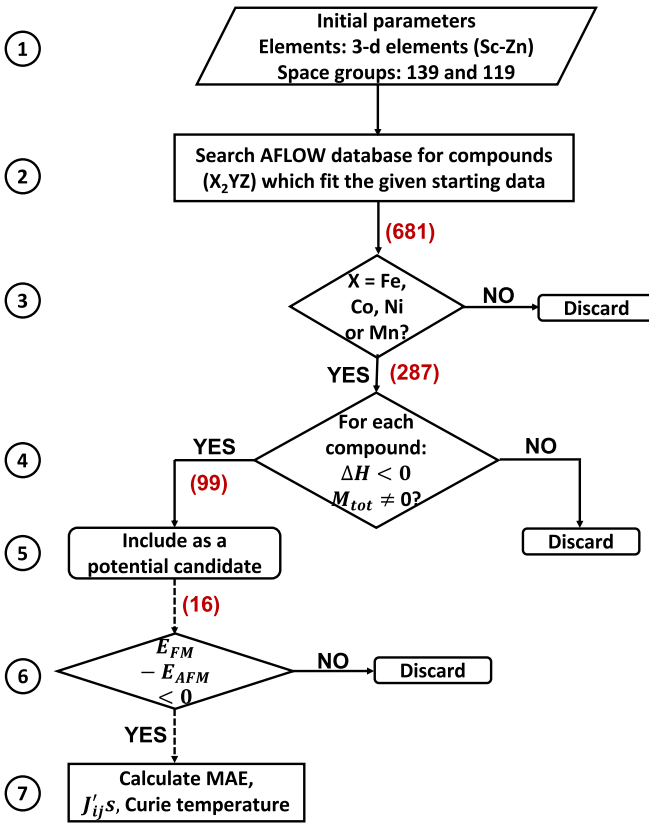
FIG. 2. Flowchart describing a detailed procedure to select the systems for our study (steps 1–5) using the AFLOW database followed by a quick summary of DFT + MC steps for the selected systems (steps 6–7). The number of compounds found after each step is given in parentheses. For DFT calculations in step 6, we ensured that there were no duplicate entries and further restricted the pool to those alloys having magnetization larger than 1.0 T. Dashed arrows indicate that only key steps are included here.

are used to reduce the statistical noise in our data. At each temperature, 50 000 steps are used to thermally equilibrate the system, and statistical averages of physical quantities are taken over the next 50 000 steps. A heating cycle is used to calculate the transition temperature with a step size of 20 K in the vicinity of the magnetic transition.

III. RESULTS AND DISCUSSION

A. High-throughput systems selection

We used the electronic structure database Automatic Flow (AFLOW) [38,39]—containing more than 3.5×10^6 material entries—to search for tetragonal Heusler alloys which are stable with negative formation of enthalpy ΔH and have magnetization larger than or equal to 1.0 T. We focused on X_2YZ-type alloys with $X =$ Mn, Fe, Co, or Ni and both Y and Z belonging to the $3d$ group from Sc to Zn; that is, we included only $3d$ transition metals in our search. Both standard and inverse Heusler structures (space groups 139 and 119, respectively) are included [40]. A flowchart summarizing our selection procedure is depicted in Fig. 2. In Table I, we have tabulated all the alloys which satisfied our initial filtering

TABLE I. List of all "eligible" X_2YZ alloys extracted from the AFLOW database including their structural parameters obtained from the database. The fourth column lists the magnetic ordering (MO), and the fifth and sixth columns list the total magnetic moment in different units for each compound calculated using DFT. The last column gives the status of the system with regard to further analysis: ✗, AFM ordering; ∗, complex spin ordering; C, cubic structure energetically favored; ∉, small MAE values. All these criteria exclude these alloys from further analysis, whereas ✓ indicates (meta)stable tetragonal and FM phases with large MAE values suitable for full analysis, and alloys marked with ✓ are discussed further in Sec. III B.

Compound	a (Å)	c/a	MO	M_{tot} (μ_B/f.u.)	M_{tot} (T)	Status
Mn$_2$NiTi	5.97	1.48	AFM	0.0	0.0	✗
Mn$_2$TiZn	6.01	1.37	FM	4.73	1.01	∗
Fe$_2$CoNi	5.66	1.33	FM	7.34	1.88	∉
Fe$_2$CoTi	5.83	1.65	FM	5.18	1.22	✓
Fe$_2$CoV	5.70	1.51	FM	4.21	1.06	✓
Fe$_2$MnTi	5.81	1.01	FM	4.16	1.00	∉
Fe$_2$NiSc	6.03	1.63	FM	5.06	1.08	∉
Fe$_2$NiTi	5.85	1.57	FM	4.50	1.05	✓
Fe$_2$NiZn	5.76	1.47	FM	5.59	1.36	✓
Co$_2$FeSc	5.97	1.01	FM	4.99	1.09	C
Co$_2$FeTi[a]	5.81	1.59	FM	4.33	1.03	C
Co$_2$FeZn	5.70	1.02	FM	4.91	1.24	C
Ni$_2$CoFe	5.61	1.45	FM	5.62	1.49	✓
Ni$_2$FeCu	5.65	1.36	FM	3.92	1.01	∉
Ni$_2$MnCu	5.69	1.33	AFM	0.0	0.0	✗
Ni$_2$MnZn	5.77	1.22	AFM	0.0	0.0	✗

[a]All these compounds except Co$_2$FeTi have the standard Heusler phase.

criteria described in steps 1–4 and used for DFT calculations in step 6 in Fig. 2. We also list the corresponding lattice constants for the cubic phase and c/a values obtained from the database.

We further analyzed each of the short-listed structures in the following way. First we performed DFT calculations to check the stability of ferromagnetic (FM) ordering versus antiferromagnetic (AFM) ordering (step 6 in Fig. 2). The corresponding low-energy spin ordering is listed in the fourth column of Table I. For the alloys found to be stable in FM ordering, we have listed the total magnetization M_{tot} obtained from our calculations in the fifth and sixth columns of Table I. Our values agree well with those reported in the AFLOW database, and all the systems indeed have large magnetic moments. We exclude those alloys for which the AFM state is more stable (marked with ✗) from further analysis.

Most conventional Heusler alloys undergo a structural phase transition between cubic and tetragonal phases depending on the constituent elements and applied strain. We have included those alloys which have a negative ΔH in the tetragonal phase (T phase), but this does not ensure that the most stable phase is indeed tetragonal, and not cubic (see Ref. [40]). Therefore, for the alloys with the FM ordering, we calculated the structural stability in the presence of tetragonal deformation. We keep the volume constant at the reference structure
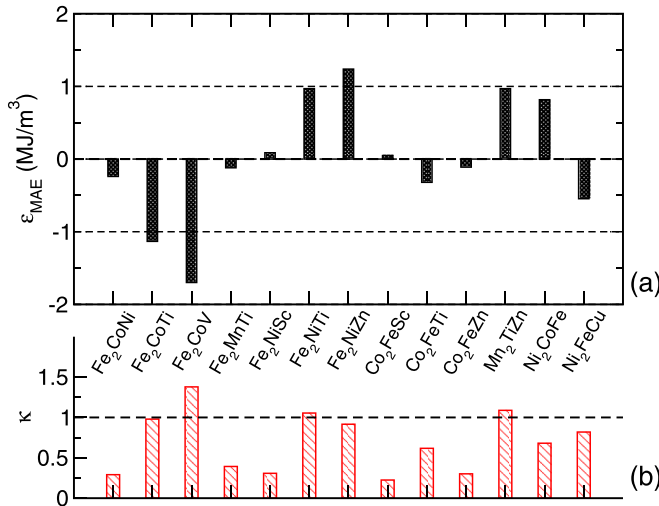
FIG. 3. For all alloys which are found to be ferromagnetic (see Table I), (a) MAE values calculated using Eq. (1) and (b) magnetic hardness parameter κ values calculated using Eq. (3) are given.

obtained from the database as we vary the ratio c/a from 0.8 to 1.7 for both standard and inverse phases (discussed in more detail for a few selected alloys later). From this analysis, we confirm that for $X = $ Fe and Ni, the tetragonal phases considered are indeed stable in the T phase or have a local minimum and so could be stabilized by either strain or deposition on a substrate. For $X = $ Co, cubic structures are energetically far more favorable, which is similar to what is observed for traditional Co-based Heusler alloys [41]. For Mn$_2$TiZn, the T phase has a very shallow minimum and also shows a tendency towards a more complex ferrimagnetic or AFM ordering with varying ratio c/a. Therefore it is not a suitable material as a permanent magnet.

In the next step we calculated the magnetocrystalline anisotropy energy for these alloys using Eq. (1). The corresponding results are given in Fig. 3(a). Furthermore, using the calculated $\mathcal{E}_{\text{MAE}}$ and the total magnetic moments, we can estimate the magnetic hardness parameter κ defined as [42]

$$\kappa = \sqrt{\frac{|\mathcal{E}_{\text{MAE}}|}{\mu_0 M_s^2}}. \qquad (3)$$

Here, $\mu_0 = 4\pi \times 10^{-7}$ J A^{-2} m^{-1} is the vacuum magnetic permeability, and M_s is the saturation magnetization expressed in units of A m^{-1}, such that κ is a dimensionless quantity. Typically, $\kappa \gtrsim 1$ is considered as a threshold for hard magnets [42]. The calculated κ values are given in Fig. 3(b). We find that Fe$_2$NiZn, Fe$_2$NiTi, Mn$_2$TiZn, and Ni$_2$CoFe alloys have large and positive MAE values indicating a preference to have out-of-plane magnetization. These alloys correspondingly show κ close to 1 with the exceptional case of Ni$_2$CoFe with $\kappa \sim 0.7$, which results from its much larger magnetization. Therefore we will further investigate all these alloys except Mn$_2$TiZn because of its complex spin ordering. Two alloys, Fe$_2$CoTi and Fe$_2$CoV, also have large but negative MAE, which indicates that in-plane magnetization is energetically favored as well as κ close to 1. Therefore these two alloys may also be interesting for applications other than

permanent magnets and are included in our subsequent analysis. Ni$_2$FeCu alloy has a high κ value of 0.8 but rather low $\mathcal{E}_{\text{MAE}}$ of -0.55 MJ/m^3 and thus is not included as a potential candidate. All the remaining systems have much smaller MAE values of $\leqslant |0.5|$ MJ/m^3, and low κ values therefore are not technologically viable. The last column of Table I summarizes the final status of the each system based on our initial analysis of suitable candidates found in the AFLOW database.

B. Functional properties of selected alloys

We first discuss in detail our structural analysis for tetragonal phases of the selected five alloys. We performed simulations for a number of tetragonal phases for both standard and inverse structures to determine minimum energy phases. These calculations are done such that the total volume of the unit cell is kept constant at its reference tetragonal structure. In Fig. 4, we have plotted the calculated total energy as a function of c/a for the selected alloys. We shift the total energy with respect to that of the cubic standard phase of the corresponding alloy for easier comparison.

For Fe$_2$NiZn and Fe$_2$NiTi alloys, the standard tetragonal phase is energetically favorable, but this phase is very close in energy to the inverse tetragonal phase as well as to the cubic phase. For Fe$_2$NiZn, the structure obtained from AFLOW (red star in Fig. 4) is lower in energy by 1.87 meV/atom compared with the local minima for the tetragonal inverse at $c/a = 1.3$ and higher in energy by 3.99 meV/atom as compared with the inverse cubic structure, whereas for Fe$_2$NiTi, the structure from AFLOW is the most stable structure with the corresponding energy differences of 4.37 meV/atom with the inverse tetragonal phase at $c/a = 1.5$ and 18.4 meV/atom with the inverse cubic phase; these energy scales are clearly indicated in Fig. 4(f). Another interesting feature of the inverse phase energy landscape for both the alloys is that from the cubic phase to the compressive strain minimum it is almost flat with a very small energy barrier to transform from one phase to another. We have confirmed that the volume of the inverse phase does not significantly vary from that of the standard phase and small changes in volume do not affect the energy landscape. We note that these are zero-temperature calculations, but at room temperature (equivalent to about 25 meV) the corresponding free-energy landscape may differ. Moreover, alloy phases will depend on and can be controlled by synthesis conditions.

In contrast to these two alloys where the standard and inverse phases show distinct behavior, Fe$_2$CoV alloys show almost no dependence on site occupancy by Fe atoms to form either the standard or inverse phase as shown in Fig. 4(c). This implies a complete site disorder if this alloy can be formed in the Heusler phase, but it is more likely that it would form a body-centered tetragonal phase as was observed in experiments [43]. Also, overall, the cubic phase is more stable, and the tetragonal phase occurs as a local minimum for this alloy. For Fe$_2$CoTi [Fig. 4(d)], the standard T phase is in the metastable state compared with the cubic phase, and the inverse cubic phase is the overall energetically favorable state. Despite their metastable structures and in-plane magnetization, we consider both Fe$_2$CoZ alloys due to their high MAE values and also because it has been shown
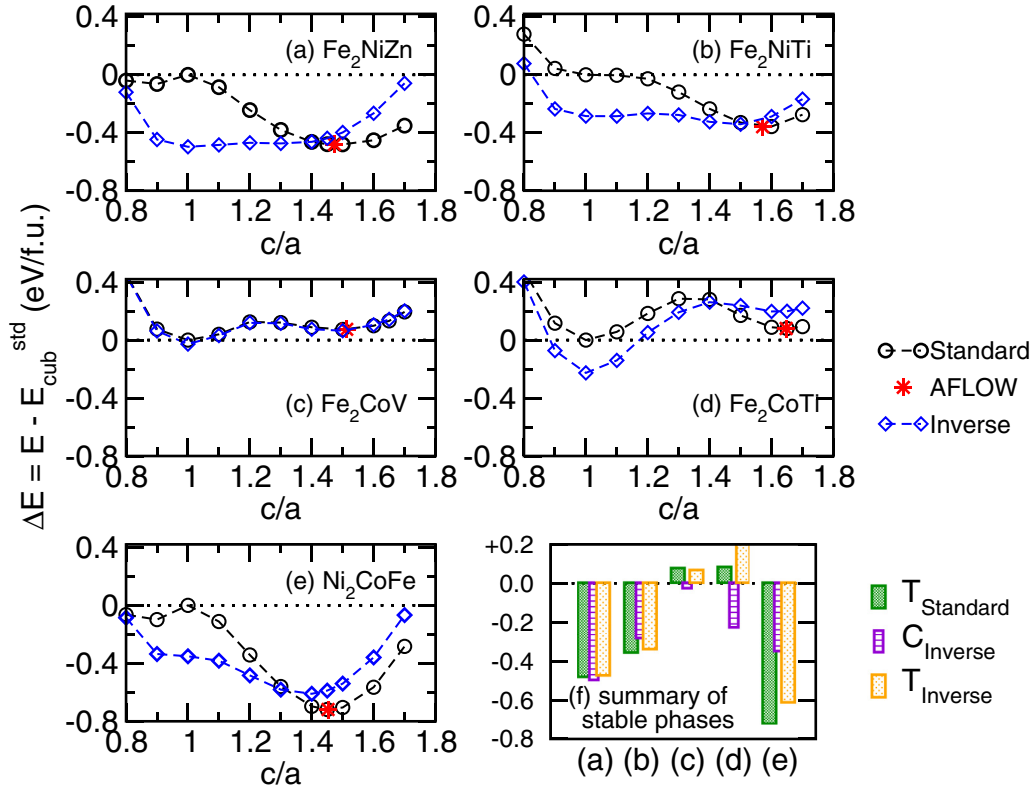
FIG. 4. Stability of tetragonal phases with respect to the cubic standard phase: Here the energy difference between a distorted structure and the cubic standard phase ΔE is plotted as a function of c/a for Fe$_2$NiZn (a), Fe$_2$NiTi (b), Fe$_2$CoV (c), Fe$_2$CoTi (d), and Ni$_2$CoFe (e). The results are shown for both standard and inverse phases along with the structure reported in the AFLOW database. (f) For easier comparison of energy scales, we summarize the ΔE values for the cubic and tetragonal phases at the potential well. In all cases, the tetragonal standard phase (green bars) corresponds to the AFLOW structure.

experimentally that doping can be used to control the sign of MAE for V-doped Fe-Co alloys [25]. For Ni$_2$CoFe [see Fig. 4(e)], the tetragonal phase from AFLOW is indeed the most stable phase observed with the inverse tetragonal phase at $c/a = 1.4$ lying 27.2 meV/atom higher in energy.

Next, we study finite-temperature magnetic properties for the selected five alloys in their tetragonal standard phase corresponding to the AFLOW structure. To map each system on the Heisenberg model, the pairwise exchange interactions J_{ij} were computed for all the alloys under study; see Fig. 5 . Note that we have calculated the pairwise interactions between all four sites within the unit cell up to a distance of $4.5a$ even though we have only shown here those interactions for which the largest interaction was $\geqslant 1$ meV for brevity. As expected, we observe that the nearest-neighbor interactions are the largest in magnitude and positive, i.e., FM coupling. Such strong nearest-neighbor interactions arise from the overlapping $3d$ orbitals. Often, larger values of J_{ij} for the nearest neighbor result in a high Curie temperature. However, note that the sign of the interactions changes from positive to negative depending on the distance, which implies a competition between FM and AFM coupling within the system which may impact the overall temperature dependence.

For $Z =$ Zn and Ti alloys, the interactions of Z with X and Y are typically negligible and would not contribute to the magnetic properties of the system. However, for $Z =$ V [see Fig. 5(d)] we observe strong AFM coupling between

nearest-neighbor Fe-V and Co-V of the same order of magnitude as the leading FM coupling between Fe-Fe and Fe-Co. These trends can be understood by looking at the local atomic moments for each alloy tabulated in Table II. Therefore, for a uniform description for all the alloys, we retain J_{ij}'s for all four sites to describe each system. Also note that the Ni$_2$CoFe alloy differs from the other alloy systems because this alloy contains only magnetic $3d$ metals and therefore results in all FM nearest-neighbor interactions, whereas in the remaining alloys there is an AFM coupling between Z and X similar to that observed in conventional Heusler alloys.

TABLE II. Local moments on different atomic sites for the selected X_2YZ alloys given in μ_B. Note that the two sites occupied by X atoms for these alloys are equivalent and have the same moment. Similar to the conventional Heusler alloys, the first four alloys' Z atoms (Ti, V, or Zn) have an induced moment with opposite sign, which is also reflected in the J_{ij}'s shown in Fig. 5.

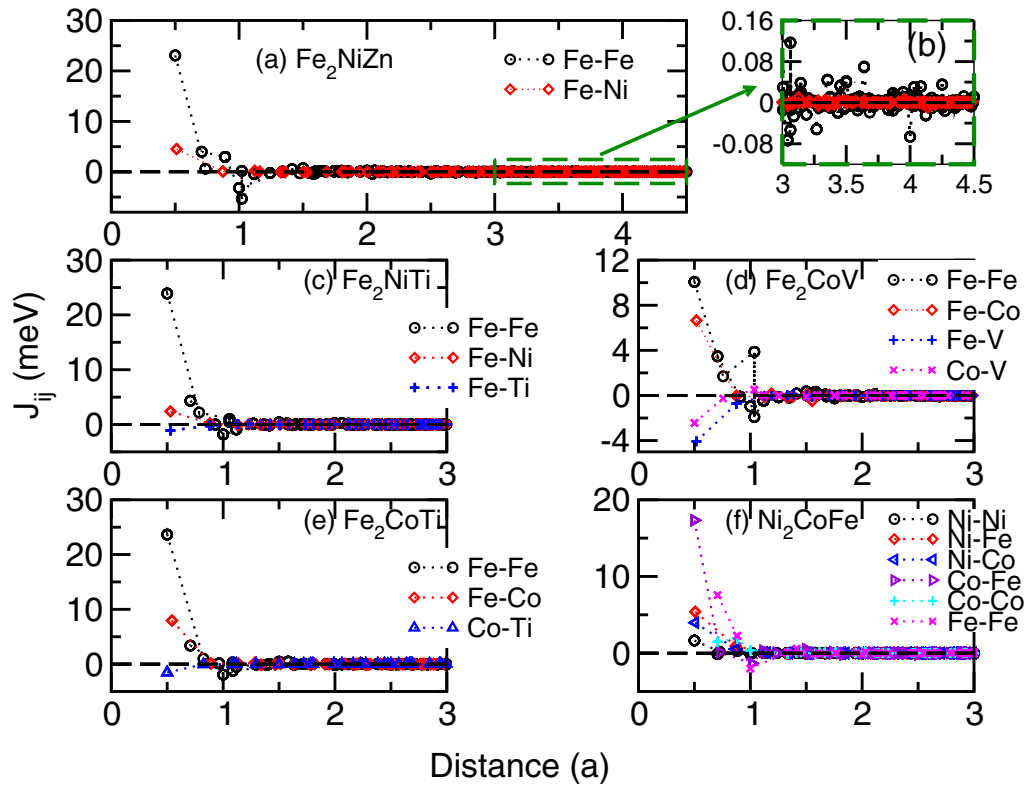| Alloy	M_X	M_Y	M_Z
Fe$_2$NiZn	2.59	0.56	−0.06
Fe$_2$NiTi	2.32	0.36	−0.33
Fe$_2$CoV	2.05	1.09	−0.79
Fe$_2$CoTi	2.33	1.05	−0.35
Ni$_2$CoFe	0.69	1.69	2.76

FIG. 5. Calculated pairwise exchange interaction J_{ij} for Fe_2NiZn (a), Fe_2NiTi (c), Fe_2CoV (d), Fe_2CoTi (e), and Ni_2CoFe (f): It is plotted as a function of distance between sites i and j given in units of the lattice constant of that alloy. A positive J_{ij} sign corresponds to the ferromagnetic coupling between atoms at i and j, whereas a negative sign corresponds to the AFM coupling. Note that the scale is different for the y axis in each panel. In (b), we have zoomed in on slowly decaying interactions at larger distances for Fe_2NiZn as an example; for other systems, we have truncated the plots at $3a$ for clarity.

The magnitude of J_{ij} decreases as the distance between the sites increases for all i and j as is expected. However, the reduction in magnitude is rather slow, and even at distances of around $3a$ (corresponding to about 15 Å), we observe significant nonzero J_{ij} values. Use of a dense k mesh ensures that we do not see any noise. As an example, in Fig. 5(b) we have zoomed in on the tail part of the J_{ij}'s for Fe_2NiZn between $3a$ and $4.5a$. Note that the values are of the order of 0.1 meV and vary between FM and AFM coupling. It has been reported that these oscillating long-range interactions originate from Ruderman-Kittel-Kasuya-Yosida interactions mediated via conduction electrons [44]. Similar behavior is observed for all the systems considered here (not shown), and exclusion of these large-distance interactions can impact simulations of finite-temperature properties as discussed later. Similar long tails for exchange interactions have been reported for conventional Heusler alloys as well [36].

To obtain the finite-temperature properties of the alloys, we fed the J_{ij}'s to the Heisenberg model given in Eq. (2). The resulting total magnetic moments of the system M_{tot} as a function of temperature are plotted in Fig. 6. As expected, M_{tot} decreases slowly as temperature increases due to the random orientations of the magnetic moment of each individual atom at different sites arising from thermal fluctuations. As a result, the material undergoes a second-order phase transition to a paramagnetic phase at high temperatures. Note that for the alloys under study the magnetic transition occurs at much higher

temperature than the room temperature. The calculated Curie temperature T_c which corresponds to the peak in susceptibility from the magnetization curves (not shown here) is highest for Ni_2CoFe at 740 K followed by Fe_2NiTi (620 K) and Fe_2CoTi (600 K) and then Fe_2NiZn (520 K) and Fe_2CoV (500 K).

Based solely on the largest observed FM interaction, we would expect the largest T_c for Fe_2NiTi, Fe_2NiZn, or Fe_2CoTi. However, this strong FM coupling is counterbalanced by AFM coupling among next-nearest neighbors, and the largest T_c is observed for Ni_2CoFe, for which all leading coupling terms are FM because of the presence of all magnetic metals and AFM coupling is much smaller. The strongest effect of such competition is observed for Fe_2CoV, in which strong AFM coupling of vanadium with Fe and Co [Fig. 5(d)] reduces both the Curie temperature and the total magnetization at zero temperature.

These results correspond to the inclusion of J_{ij}'s corresponding to all the neighboring sites within a distance of $4.5a$. To establish the effect of long-range interactions on the temperature dependence, we have compared the temperature dependence of M_{tot} for Fe_2NiZn when we exclude J_{ij}'s for sites at a distance larger than $3a$ as shown in the inset of Fig. 6. Note that near the transition temperature there is a lot of statistical noise in the data and the system does not undergo a smooth transition. Such noise typically implies that the system has competing phases and is not able to reach equilibrium. For MC simulations, this may arise from either inadequate
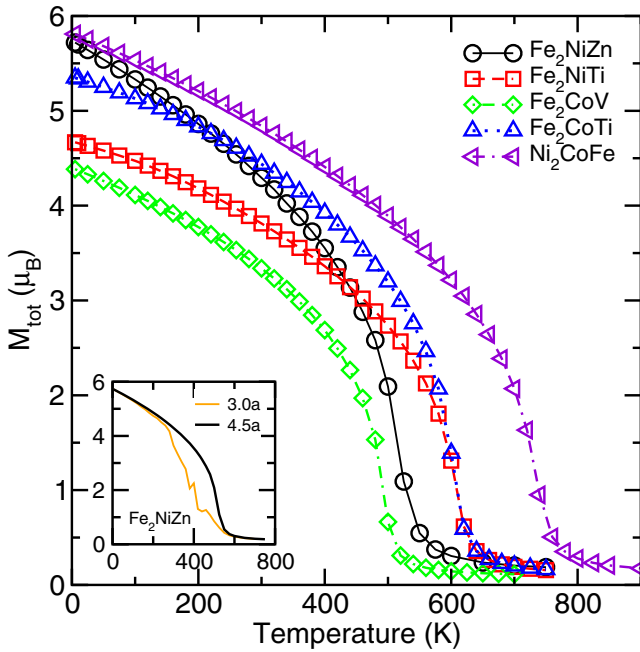
FIG. 6. Curie temperature calculation: The total magnetic moment as a function of temperature obtained from Monte Carlo simulations is plotted for different alloys. The inset compares the corresponding data for Fe_2NiZn calculated by including only short-range J_{ij} interactions within the model.
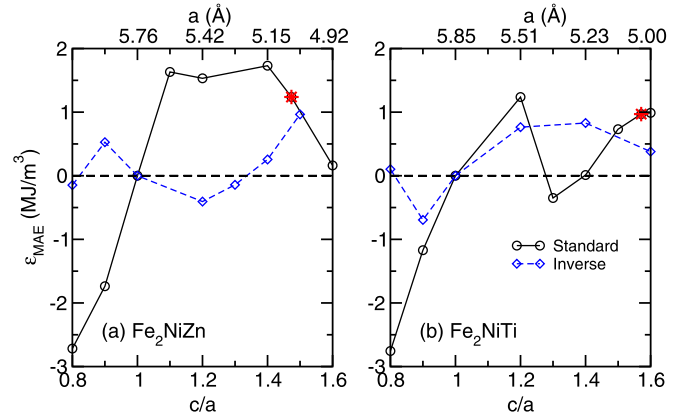

FIG. 7. Effect of tetragonality on magnetic anisotropy: We have plotted here the calculated MAE for Fe_2NiZn (a) and Fe_2NiTi (b) as a function of the ratio c/a for both standard and inverse phases, and the corresponding in-plane lattice constants a are indicated at the top of the plots. The AFLOW structure is highlighted with a red star, and the corresponding MAE values are those shown in Fig. 3.

sampling or because "model material" does not describe the "real" system completely. Additional tests showed that the noise is not reduced by increasing either the system size, the simulation time, or the number of ensembles to improve the quality of the data. However, including long-range interactions results in a smoother transition confirming that the long-range nature of exchange interactions is essential to include in the Heisenberg model for these systems. This noise can be explained by the competing FM and AFM coupling present at larger distance shown in Fig 5(b). Therefore we conclude that for materials containing $3d$ transition metals it is important to check the convergence of long-distance interactions for better predictive power of simulations.

C. Tuning of MAE

As discussed at the beginning of Sec. III B, the alloys studied here show two minima (either global or local) in the cubic phase and the tetragonal phase with certain compressive strain. These two structural phases and the standard and inverse phases arising from chemical site ordering are shown to have small energy differences; therefore it should be possible to achieve these phases by applying strain or using different substrates for growing thin films. Typically for $3d$ elements, the d orbitals lying near the Fermi level contribute the most to MAE [45], and the shape and position of d orbitals are quite sensitive to the structure, strain, and chemical environment for the metal, which in turn means that MAE too is sensitive to these changes. Therefore, next, we examine the effect of tetragonality and site occupancy on the MAE values for the most promising alloys: Fe_2NiZn and Fe_2NiTi. Note that

even though Ni_2CoFe has the highest T_c and is quite stable in its tetragonal phase compared with the cubic phase, its constituent elements tend to form binary alloys with several competing phases [21] making synthesis of Ni_2CoFe in the Heusler structure very difficult. These arguments based on existing binary phase diagrams are further confirmed by calculation of the phonon dispersion for these three alloys done to check the dynamic stability of each phase; see Supplemental Material [46] for details. This alloy system therefore would require more detailed study based on free-energy analysis and is not considered for strain tuning.

The calculated MAE values as a function of c/a are plotted in Fig. 7 for both standard and inverse phases. In agreement with earlier observations, we observe that the strain leads to changes in the magnitude of MAE and also results in rotation of the easy-plane axis from the out-of-plane to the in-plane axis for both standard and inverse phases. For inverse phases (blue diamonds), overall smaller $|\mathcal{E}_{MAE}|$ is observed for both strain regimes. Significantly for applications, in the vicinity of stable AFLOW structures (shown with a red star) values of MAE are comparable for standard and inverse phases. This indicates that site disorder should not affect the MAE for these alloys.

For both alloys in the standard phase, the MAE is negative for tensile strains implying in-plane magnetization, its magnitude increases with increasing strain. However, we observe highly nonmonotonic trends in MAE as we go from tensile ($c/a < 1$) to compressive ($c/a > 1$) strain. For the Fe_2NiZn standard phase, the tetragonal phases with c/a between 1.1 and 1.5 have a large positive MAE of $>1\,MJ/m^3$ which is very promising for applications, whereas for Fe_2NiTi, the positive MAE observed for the ground state ($c/a = 1.57$) is reduced almost to zero at $c/a = 1.4$ before going to a large positive value of $1.2\,MJ/m^3$ at $c/a = 1.2$. This trend implies that very accurate control of growth or preparation conditions would be needed for potential applications for the latter alloy. For conventional Ni-based Heusler alloys, a density of states analysis based on the occupation and position of d orbitals worked

well [8]; however, for the alloys studied here the correlation is more complex and not obvious. Based on the in-plane lattice constants for cubic and tetragonal phases (indicated as the top x axis in Fig. 7), we suggest a few suitable substrates—GaAs having lattice constant 4.00 Å for cubic phases or Cu with 3.61 Å for tetragonal phases at the local minima (see Table 1 in Ref. [47])—which have a small lattice mismatch calculated with respect to $a_p = a/\sqrt{2}$ and therefore can be used to grow the "correct" phase for tuning anisotropy.

IV. SUMMARY AND CONCLUSIONS

We used a combination of a high-throughput database search, density functional theory calculations, and Monte Carlo simulations to study a new subclass of Heusler alloys—all-3d Heusler alloys—as potential candidates for permanent magnets. After application of the first filters with a set of criteria we obtained about 20 systems with tetragonal symmetry and high magnetic moments in the AFLOW database. For these alloys, we performed a thorough examination of the preferred easy-plane axis and Curie temperatures to find three potential candidates—Fe$_2$NiZn, Fe$_2$NiTi, and Ni$_2$CoFe—with magnetocrystalline anisotropy of the order of 1 MJ/m^3, with preferred out-of-plane magnetization, and which remain ferromagnetic for at least 200 K above room temperature. For Fe$_2$NiZn and Fe$_2$NiTi, the energy landscape is rather flat implying that strain can stabilize the tetragonal phase. We further showed for these alloys that strain engineering is a viable option to further tune their anisotropy and site disorder between Fe and Ni would not reduce MAE significantly. A few conventional Heusler alloys show potential for spintronics applications; however, we obtain low spin polarization values for these alloys (see Supplemental Material [46]). Therefore these three alloys do not appear viable for spintronics applications.

We also found two alloys—Fe$_2$CoV and Fe$_2$CoTi—with high Curie temperature and large MAE, but with an in-plane easy axis. These alloys are good candidates for further studies to examine whether alloying and/or doping can be used to rotate the easy axis. Moreover, some of the alloys which did not pass our initial filters for permanent magnets showed some promising properties and could be studied further for applications such as magnetocalorics.

Our study opens up a class of rare-earth free permanent magnets with extensive potential possible via thin-film growth for strain tuning. We would like to note that due to the absence of heavy metals, there is admittedly a limit to the largest anisotropy obtained within this class of Heusler alloys. However, there exists a large market for intermediate applications of permanent magnets which do not require strong anisotropy. We believe that use of these magnets for such applications can result in an overall reduction in dependence on the rare-earth metals.

[1] O. Gutfleisch, M. A. Willard, E. Brück, C. H. Chen, S. G. Sankar, and J. P. Liu, Magnetic materials and devices for the 21st century: Stronger, lighter, and more energy efficient, Adv. Mater. **23**, 821 (2011).

[2] M. J. Kramer, R. W. McCallum, I. A. Anderson, and S. Constantinides, Prospects for non-rare earth permanent magnets for traction motors and generators, JOM **64**, 752 (2012).

[3] L. H. Lewis and F. Jiménez-Villacorta, Perspectives on permanent magnetic materials for energy conversion and power generation, Metallurg. Mater. Trans. A **44**, 2 (2013).

[4] G. Bailey, N. Mancheri, and K. Van Acker, Sustainability of permanent rare earth magnet motors in (H)EV industry, J. Sustainable Metall. **3**, 611 (2017).

[5] J. H. van Vleck, On the Anisotropy of Cubic Ferromagnetic Crystals, Phys. Rev. **52**, 1178 (1937).

[6] *Heusler Alloys: Properties, Growth, Applications*, edited by C. Felser and A. Hirohata, Springer Series in Material Science Vol. 222 (Springer, New York, 2016).

[7] Y.-I. Matsushita, G. Madjarova, J. K. Dewhurst, S. Shallcross, C. Felser, S. Sharma, and E. K. U. Gross, Large magnetocrystalline anisotropy in tetragonally distorted Heuslers: a systematic study, J. Phys. D **50**, 095002 (2017).

[8] H. C. Herper, Ni-based Heusler compounds: How to tune the magnetocrystalline anisotropy, Phys. Rev. B **98**, 014411 (2018).

[9] Q. Gao, I. Opahle, O. Gutfleisch, and H. Zhang, Designing rare-earth free permanent magnets in Heusler alloys via interstitial doping, Acta Mater. **186**, 355 (2020).

[10] V. V. Sokolovskiy, O. N. Miroshkina, V. D. Buchelnikov, and M. E. Gruner, Impact of local arrangement of Fe and Ni on the phase stability and magnetocrystalline anisotropy in Fe-Ni-Al Heusler alloys, Phys. Rev. Mater. **6**, 025402 (2022).

[11] V. G. de Paula and M. S. Reis, All-d-metal *full* Heusler alloys: A novel class of functional materials, Chem. Mater. **33**, 5483 (2021).

[12] Z. Y. Wei, E. K. Liu, J. H. Chen, Y. Li, G. D. Liu, H. Z. Luo, X. K. Xi, H. W. Zhang, W. H. Wang, and G. H. Wu, Realization of multifunctional shape-memory ferromagnets in all-d-metal Heusler phases, Appl. Phys. Lett. **107**, 022406 (2015).

[13] Z. Y. Wei, E. K. Liu, Y. Li, X. L. Han, Z. W. Du, H. Z. Luo, G. D. Liu, X. K. Xi, H. W. Zhang, W. H. Wang, and G. H. Wu, Magnetostructural martensitic transformations with large volume changes and magneto-strains in all-d-metal Heusler alloys, Appl. Phys. Lett. **109**, 071904 (2016).

[14] Z. Ni, Y. Ma, X. Liu, H. Luo, H. Liu, and F. Meng, Electronic structure, magnetic properties and martensitic transformation in all-d-metal Heusler alloys Zn$_2$YMn (Y = Fe, Co, Ni, Cu), J. Magn. Magn. Mater. **451**, 721 (2018).

[15] Z. Ni, X. Guo, X. Liu, Y. Jiao, F. Meng, and H. Luo, Understanding the magnetic structural transition in all-d-metal Heusler alloy Mn$_2$Ni$_{1.25}$Co$_{0.25}$Ti$_{0.5}$, J. Alloys Compd. **775**, 427 (2019).

[16] K. Özdoğan, I. V. Maznichenko, S. Ostanin, E. Şaşıoğlu, A. Ernst, I. Mertig, and I. Galanakis, High spin polarization in all-3d-metallic Heusler compounds: the case of Fe$_2$CrZ and Co$_2$CrZ (Z = Sc,Ti,V), J. Phys. D **52**, 205003 (2019).

[17] S. Samanta, S. Ghosh, and K. Mandal, Observation of giant exchange bias effect in Ni–Mn–Ti all-d-metal Heusler alloy, J. Phys.: Condens. Matter **34**, 105801 (2022).

[18] A. Aznar, A. Gràcia-Condal, A. Planes, P. Lloveras, M. Barrio, J.-L. Tamarit, W. Xiong, D. Cong, C. Popescu, and L. Mañosa, Giant barocaloric effect in all-d-metal Heusler shape memory alloys, Phys. Rev. Mater. **3**, 044406 (2019).

[19] S. Samanta, S. Ghosh, S. Chatterjee, and K. Mandal, Large magnetocaloric effect and magnetoresistance in Fe-Co doped Ni$_{50-x}$(FeCo)$_x$Nn$_{37}$Ti$_{13}$ all-d-metal Heusler alloys, J. Alloys Compd. **910**, 164929 (2022).

[20] S. Samanta, S. Chatterjee, S. Ghosh, and K. Mandal, Large reversible magnetocaloric effect and magnetoresistance by improving crystallographic compatibility condition in Ni(Co)-Mn-Ti all-d-metal Heusler alloys, Phys. Rev. Mater. **6**, 094411 (2022).

[21] *Ferromagnetic Materials: A Handbook on the Properties of Magnetically Ordered Substances*, edited by E. P. Wohlfarth (North-Holland, Amsterdam, 1980), Vol. 2, Chap. 2.

[22] T. Burkert, L. Nordström, O. Eriksson, and O. Heinonen, Giant Magnetic Anisotropy in Tetragonal FeCo Alloys, Phys. Rev. Lett. **93**, 027203 (2004).

[23] K. Hyodo, Y. Kota, and A. Sakuma, Theoretical evaluation of perpendicular magnetic anisotropy of bct-Fe$_{50}$Co$_{50}$ stacked on Rh, J. Magn. Soc. Jpn. **39**, 37 (2015).

[24] F. Yildiz, M. Przybylski, X.-D. Ma, and J. Kirschner, Strong perpendicular anisotropy in Fe$_{1-x}$Co$_x$ alloy films epitaxially grown on mismatching Pd(001), Ir(001), and Rh(001) substrates, Phys. Rev. B **80**, 064415 (2009).

[25] T. Hasegawa, T. Niibori, Y. Takemasa, and M. Oikawa, Stabilisation of tetragonal FeCo structure with high magnetic anisotropy by the addition of V and N elements, Sci. Rep. **9**, 5248 (2019).

[26] Y. Du, G. Z. Xu, X. M. Zhang, Z. Y. Liu, S. Y. Yu, E. K. Liu, W. H. Wang, and G. H. Wu, Crossover of magnetoresistance in the zero-gap half-metallic Heusler alloy Fe$_2$CoSi, Europhys. Lett. **103**, 37011 (2013).

[27] A. K. Jana, M. M. Raja, J. A. Chelvane, P. Ghosal, and S. N. Jammalamadaka, Thickness dependent domain wall dynamics in Fe$_2$CoSi thin films, J. Magn. Magn. Mater. **521**, 167528 (2021).

[28] S. Wurmehl, G. H. Fecher, H. C. Kandpal, V. Ksenofontov, C. Felser, H.-J. Lin, and J. Morais, Geometric, electronic, and magnetic structure of Co$_2$FeSi: Curie temperature and magnetic moment measurements and calculations, Phys. Rev. B **72**, 184434 (2005).

[29] P. J. Brown, K. U. Neumann, P. J. Webster, and K. R. A. Ziebeck, The magnetization distributions in some Heusler alloys proposed as half-metallic ferromagnets, J. Phys.: Condens. Matter **12**, 1827 (2000).

[30] H. C. Herper and A. Grünebohm, Tuning the magnetic anisotropy of NiPtMnGa by substitution and epitaxial strain, IEEE Trans. Magn. **55**, 2100804 (2019).

[31] G. Kresse and J. Furthmüller, Efficiency of ab-initio total energy calculations for metals and semiconductors using a plane-wave basis set, Comput. Mater. Sci. **6**, 15 (1996).

[32] G. Kresse and D. Joubert, From ultrasoft pseudopotentials to the projector augmented-wave method, Phys. Rev. B **59**, 1758 (1999).

[33] J. M. Wills, M. Alouani, P. Andersson, A. Delin, O. Eriksson, and O. Grechnyev, Introduction to electronic structure theory, in *Full-Potential Electronic Structure Method: Energy and Force Calculations with Density Functional and Dynamical Mean Field Theory* (Springer, Berlin, 2010), pp. 25–34.

[34] X. Wang, D. sheng Wang, R. Wu, and A. Freeman, Validity of the force theorem for magnetocrystalline anisotropy, J. Magn. Magn. Mater. **159**, 337 (1996).

[35] A. Liechtenstein, M. Katsnelson, V. Antropov, and V. Gubanov, Local spin density functional approach to the theory of exchange interactions in ferromagnetic metals and alloys, J. Magn. Magn. Mater. **67**, 65 (1987).

[36] P. Entel, A. Dannenberg, M. Siewert, H. C. Herper, M. E. Gruner, D. Comtesse, H.-J. Elmers, and M. Kallmayer, Basic properties of magnetic shape-memory materials from first-principles calculations, Metallurg. Mater. Trans. A **43**, 2891 (2012).

[37] O. Eriksson, A. Bergman, L. Bergqvist, and J. Hellsvik, *Ab-initio Spin-Dynamics: Foundations and Applications* (Oxford University Press, Oxford, 2017).

[38] https://aflow.org

[39] F. Rose, C. Toher, E. Gossett, C. Oses, M. B. Nardelli, M. Fornari, and S. Curtarolo, AFLUX: The LUX materials search API for the AFLOW data repositories, Comput. Mater. Sci. **137**, 362 (2017).

[40] Note that here the exclusion of cubic Heusler alloys (space groups 225 and 216) from our search criteria can be a drawback because even metastable tetragonal phases with negative ΔH will be included in our list even when the cubic phase is the most stable phase. However, we look for such a possibility.

[41] S. Trudel, O. Gaier, J. Hamrle, and B. Hillebrands, Magnetic anisotropy, exchange and damping in cobalt-based full-Heusler compounds: an experimental review, J. Phys. D **43**, 193001 (2010).

[42] J. M. D. Coey, Hard magnetic materials: A perspective, IEEE Trans. Magn. **47**, 4671 (2011).

[43] K. Takahashi, M. Sakamoto, K. Kumagai, T. Hasegawa, and S. Ishio, Uniaxial magnetic anisotropy of tetragonal FeCoV and FeCoVC films, J. Phys. D **51**, 065005 (2018).

[44] E. Şaşıoğlu, L. M. Sandratskii, and P. Bruno, Role of conduction electrons in mediating exchange interactions in Mn-based Heusler alloys, Phys. Rev. B **77**, 064417 (2008).

[45] H. Takayama, K.-P. Bohnen, and P. Fulde, Magnetic surface anisotropy of transition metals, Phys. Rev. B **14**, 2287 (1976).

[46] See Supplemental Material at http://link.aps.org/supplemental/10.1103/PhysRevB.107.174402 for the phonon band dispersion and spin polarized density of states data for the tetragonal phases of Fe$_2$NiZn, Fe$_2$NiTi, and Ni$_2$CoFe, which support our discussion on the dynamical stability of the alloy phases and

their viability for spintronics applications, respectively. The Supplemental Material also contains Ref. [48].

[47] L. Zhu and J. Zhao, Perpendicularly magnetized Mn$_x$Ga films: promising materials for future spintronic devices, magnetic recording and permanent magnets, Appl. Phys. A **111**, 379 (2013).

[48] A. Togo and I. Tanaka, First principles phonon calculations in materials science, Scr. Mater. **108**, 1 (2015).